Investigating gas phase defects formation in late-stage solidification using a novel phase-field-crystal model

Nan Wang, Nathan Smith and Nikolas Provatas
Department of Physics, McGill University, Montreal, Québec, Canada
(Dated: April 26, 2017)

We study late stage solidification and its associated defects formation in alloy materials using a novel computational model based on the phase-field-crystal technique. It is shown that this model successfully captures several important physics that happen at the late stage of solidification including solidification shrinkage, liquid cavitation and micro-segregation in a single framework. By examining the interplay of solidification shrinkage and solute segregation, this model reveals that the formation of gas pore defects at the late stage of solidification can be accompanied by nucleation of second phase particles due to solute enrichment in the eutectic liquid driven by gas phase nucleation and growth.

Solidification of crystalline materials, particularly alloy materials, has been a topic of both theoretical and practical importance for many years [1, 2]. Extensive works have been dedicated to understanding solidification patterns and resulting microstructures [3, 4]. Near the end of the solidification process where the volume fraction of solidified dendritic network reaches 90% and above, this late stage solidification happens in highly confined interdendritic channels and separated eutectic pools [2, 4]. It has long been known that the solidification behavior at this late stage is associated with the formation defects and second phase particles. Gas phase defects, such as microporosity and hot tears, form at this stage and are imprinted into the final solidified microstructure. However, our knowledge on late stage solidification of low concentration alloys is still very limited despite of its strong impact on final material properties [5].

In classic solidification picture, this partially solidified region with a small liquid volume fraction is called mushy zone and is typically seen as a semi-solid [2]. Many experimental and theoretical studies have been dedicated to understand materials behavior in this mushy zone [6–11]. Since there is typically a density difference between the solid and the liquid melt, solidification in this confined environment has been known to generate local pressure changes due to this shrinkage effect. It has been shown in experiments that the pressure induce from solidification shrinkage may lead to porosity formation, hot tearing failure, deformation of the dendritic network and even recrystallization in solidified structure [12–15]. Niyama's criterion was developed to explain the formation of gas porosity [16]. Rappaz, Drezet and Gremaud (RDG) developed a two-phase theory that takes into account both elastic and plastic deformation of the solid confinement in the formation of hot tears [17]. The nucleation of gas phase (or cavitation) in those microstructure-scale continuum based models is typically approached by setting up a pressure threshold which can be obtained from atomic level models [18, 19]. Solidification of non-equilibrium or second phases is another important phenomenon that happens at the late stage [20]. Continuous enrichment of the confined liquid melts due to solute rejection at the solidification front (commonly known as microsegregation) leads to the formation of small secondary solid phases below the eutectic point [21–23]. Materials strength can be strongly affected by the size and distribution of those small particles [24, 25]. Based on local solute partitioning, the Gulliver-Scheil equation has been widely used to explain the solute enrichment in eutectic liquid at the late stage. However, the formation of gas phase defects (gas porosity and hot tears) and the solidification of secondary phases due to microsegregation are mainly studied in separate contexts in most previous works despite of the fact that they are all important in the late stage of solidification.

While the classic solidification theory has been very successful in predicting microstructures on the order of microns and above, its fundamental length scale is tied to the Mullins-Sekerka instability wavelength [1]. Since the size of the confined interdendritice channels and isolated liquid pools is usually associated with the primary and the secondary dendrite arm spacing which are manifestations of the Mullins-Sekerka instability wavelength, the most relevant length scale to the late stage of solidification is likely to be smaller than the length scale of the classic solidification theory. On the other end, when the liquid channels are narrowed down to the size that is comparable to the solid-liquid interface width (on the order of $1nm$), theories based on interface disjoining potentials have been developed recently to explain coalescence and bridging of grains at this last stage of solidification [5, 26]. A comprehensive understanding of the solidification behavior that happens in confined environment on the size of $10nm$ up to a few microns is still largely missing.

To investigate the confined late stage solidification and its associated phenomena such as gas phase defects formation and secondary phase formation, one needs a model that is capable to capture solute segregation, gas phase nucleation, solidification shrinkage, elastic and possible plastic deformations in the solid confinement [27]. This seemingly daunting task has been made possible by a series of recent progress in the phase-field-crystal (PFC) model [28]. Originally developed for solidification problems in pure materials, the PFC model naturally incorporates elasticity and lattice defects (like dislocations and grain boundaries) in solid state [29]. Later extensions of this modeling technique have covered alloy materials [30], solid-state structural transformation [31], and gas phase nucleation [32]. Typical length scale of PFC model is about $10 - 100nm$ which coincides with what is required to

investigate late stage solidification process. This method has been used to study dendritic crystal growth which is the dominant form of solidification at low solid volume fraction [33] and the effect of disjoining potential in grain coalescence which is the last stage of solidification[34]. Since most of the previous PFC models do not incorporate the density change in solidification and gas phase formation, studies of late stage solidification using this technique have been very limited. In this work, we formulate a novel PFC model that incorporates both solidification shrinkage and gas phase nucleation. The shrinkage induced pressure in the liquid near the solidification front is reproduced. By considering gas phase formation, it is shown that the late stage Gulliver-Scheil type microsegregation behavior in the liquid can be modified. As a result, we also demonstrate that the formation of gas porosity can be accompanied by nucleation and growth of second phase particles in eutectic pools.

The PFC model in this work is developed based on a synergy of previous alloy and gas phase models [31, 32]. The free energy functional in general is formulated using concentration filed c and dimensionless density field n as

$$F_{PFC} = F_{ideal} + F_{pair} + F_{MP}, \tag{1}$$

with the ideal part

$$F_{ideal} = \int \left[\epsilon \frac{n(\mathbf{r})^2}{2} - W_1 \frac{n(\mathbf{r})^3}{6} + W_2 \frac{n(\mathbf{r})^4}{12} \right] d\mathbf{r}, \tag{2}$$

the pair correlation part

$$F_{pair} = F_{nn} + F_{nc} + F_{cc}, \tag{3}$$

with density correlation F_{nn}, concentration correlation F_{cc}, density-concentration correlation F_{nc} and the multi-point correlation F_{MP}. The dimensionless PFC density is $n(\mathbf{r}) = (\rho - \bar{\rho})/\bar{\rho}$, and $\bar{\rho}$ is the reference fluid density around which the F is expanded. Different part of the pair correlation contribution can be written as [31]

$$F_{nn} = \int n(\mathbf{r}_1) \left\{ \int \left[\xi(c) C^{AA}(\mathbf{r}_1 - \mathbf{r}_2) + \xi(1-c) C^{BB}(\mathbf{r}_1 - \mathbf{r}_2) \right] n(\mathbf{r}_2) d\mathbf{r}_2 \right\} d\mathbf{r}_1, \tag{4}$$

$$F_{nc} = \int \zeta(c(\mathbf{r}_1)) n(\mathbf{r}_1) \left[\int \zeta(c(\mathbf{r}_2)) \chi_c(\mathbf{r}_1 - \mathbf{r}_2) n(\mathbf{r}_2) d\mathbf{r}_2 \right] d\mathbf{r}_1, \tag{5}$$

and

$$F_{cc} = \int \alpha |\nabla c|^2 d\mathbf{r}. \tag{6}$$

The contribution from multi-point correlation is

$$F_{MP} = \sum_{m=3}^{4} \frac{1}{m} \int d\mathbf{r}_1 ... d\mathbf{r}_m \chi_m(\mathbf{r}_1, ..., \mathbf{r}_m) n(\mathbf{r}_1) ... n(\mathbf{r}_m), \tag{7}$$

For the density pair correlation functions in Eq.4, we take the first peak approximation $C^{AA} = B_{x1}(q_1^2 + \nabla^2)^2$ and $C^{BB} = B_{x2}(q_2^2 + \nabla^2)^2$ with q_1 and q_2 being the firs peak position of $c = 0$ structure and $c = 1$ structure in reciprocal space. ξ is an smooth interpolation function given in ref[31]. Assuming the concentration field c changes slowly comparing with n, Eq.5 is approximated by replacing $c(\mathbf{r}_2)$ with $c(\mathbf{r}_1)$ and choosing $|\zeta(c)|^2 = \frac{u_1}{2}(c-c_0)^2 + \frac{v_1}{4}(c-c_0)^4$. The multi-point density correlations are chosen to be $\chi_3 = (a_1\epsilon + b_1)\chi(\mathbf{r}_1 - \mathbf{r}_2)\chi(\mathbf{r}_1 - \mathbf{r}_3)$ and $\chi_4 = c_1\chi(\mathbf{r}_1 - \mathbf{r}_2)\chi(\mathbf{r}_1 - \mathbf{r}_3)\chi(\mathbf{r}_1 - \mathbf{r}_4)$ with $\chi(\mathbf{k}) = e^{-\frac{\mathbf{k}^2}{2\lambda}}$ in reciprocal space as seen in Ref[32]. The density-concentration pair correlation is approximated by $\chi_c(\mathbf{k}) = e^{-\frac{\mathbf{k}^2}{2\lambda_c}}$.

Basic thermodynamic properties of this PFC model are shown in Fig.1. Model parameter ϵ serves as a temperature analog [29]. It is noted that cavitation behavior of eutectic liquid is strongly affected by dissolved gas content. The demonstrated cavitation thermodynamics in Fig.1(b) can be tuned based on different gas contents. However, the current model does not incorporate the dissolved gas concentration explicitly.

Evolutions of n and c then follow conserved variational dynamics

$$\frac{\partial n}{\partial t} = \nabla \cdot \left(M_n \nabla \frac{\delta F}{\delta n} \right) + \eta, \tag{8}$$

and

$$\bar{n} \frac{\partial c}{\partial t} = \nabla \cdot \left(\bar{n} M_c \nabla \frac{\delta F}{\delta c} \right), \tag{9}$$

with corresponding mobility M_n and M_c, a locally averaged density $\bar{n}(r) = \int n(r')\chi(r - r')dr'$, and η a stochastic noise term satisfying the fluctuation-dissipation theorem $<\eta(\mathbf{r}, t), \eta(\mathbf{r}', t')> = -2(M_n/\bar{\rho}a^d)\nabla^2\delta(\mathbf{r} - \mathbf{r}')\delta(t - t')$, where a is the lattice constant. Eq.9 is slightly different from the classic concentration dynamics seen in literature. It is clear that this generalized concentration dynamics for spatially inhomogeneous $\bar{n}$ is reduced to the classic concentration dy-

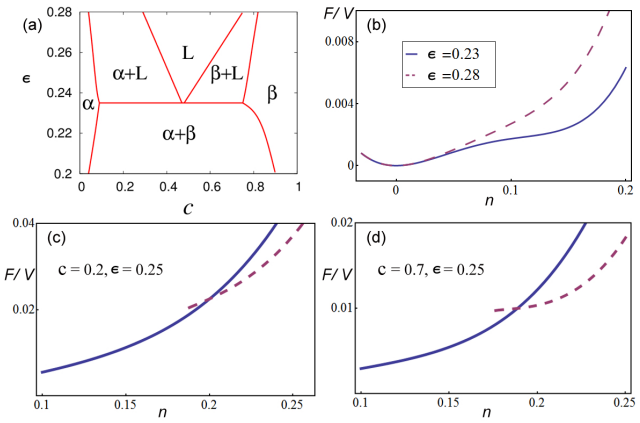

FIG. 1: Basic thermodynamic properties of the PFC model. (a) Alloy phase diagram. (b) Cavitation of eutectic liquid with concentration $c = 0.5$. (c) and (d) Solidification shrinkage of α and β solid in coexistence region. Solid state and liquid state free energy are shown in dashed line and solid line in (c) and (d) accordingly. Model parameters used here are $W_1 = 1.3$, $W_2 = 0.6$, $\alpha = 8.0$, $B_{x1} = 0.3$, $B_{x2} = 0.9$, $q_1 = \sqrt{2}$, $q_1 = 1$, $u_1 = 6.0$, $v_1 = 3.0$, $c_0 = 0.5$, $a_1 = 43$, $b_1 = -30$, $c_1 = 90$, $\lambda = \lambda_c = 0.04$.

namics when $\bar{n}$ is a constant in the system.

One important phenomenon that raises at the late stage of solidification is the pressure drop in the liquid confined by surrounding solid network. Since the solidification shrinkage happens at the solid-liquid interface, the local mass shortage at the interface needs to be feed through liquid transport. To satisfy this mass balance condition, velocity of the liquid normal to the solidification front is $v_{ln} = \beta v_n$ where v_n is the velocity of the solid-liquid interface, $\beta = (\rho_S - \rho_L)/\rho_L$, with solid density ρ_S and liquid density ρ_L, is the shrinkage factor[2]. Assuming the liquid flow in the small confined geometry is driven only by pressure gradient (Darcy's law), the pressure drop in the liquid at distance d from a large liquid reservoir is then

$$\triangle P(d) = \beta v_n \int_0^d \frac{\mu f_l}{K(f_l)} dx, \tag{10}$$

with liquid viscosity μ, mushy zone permeability K and local liquid volume fraction f_l. Eq.10 is a quasi 1-dimensional model where the effective materials property perpendicular to the interface normal is included in the liquid fraction f_l. It can be further simplified to $\triangle P(d) = \beta v_n \int_0^d g(x)dx$ with $g(x) = \mu f_l(x)/K(x)$ and boundary condition $f_l(0) = f_l^D$ where f_l^D is the upper limit of the liquid fraction from which the Darcy type flow becomes dominant. RDG formulated a hot tearing criterion by adding elastic and plastic deformations of the solid confinement [17]. The PFC model formulated in Eq.1 captures the shrinkage induced pressure drop in Eq.10 as demonstrated in Fig.2. Dependence of the peak pressure drop as functions of interface velocity v_n and shrinkage factor β are also shown.

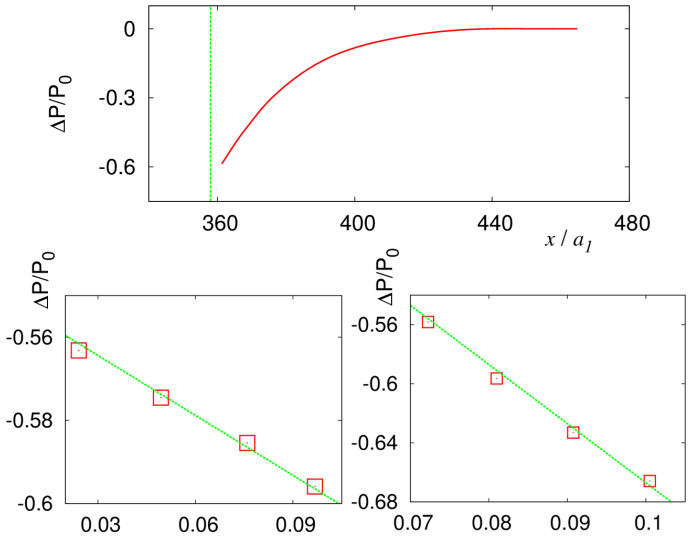

FIG. 2: Pressure drop in front of the solidifying interface. (a) Pressure drop in the liquid from solidification shrinkage. (b) Pressure drop as a function of solidification front velocity. (c) Pressure drop as a function of shrinkage factor β. P_0 is the pressure of the liquid reservoir. The green dashed line in (a) marks the solid-liquid interface. The green dashed lines in (b) and (c) are eye guidance. Figure (b) and (c) are plotted based on the peak pressure near the solidification front. Quasi 1-dimensional geometry (one unit cell along the solid-liquid interface) is used in numerics. $f_l = f_l^D$ in the reservoir. Other model parameters are given in Fig.1.

Microsegregation of solute atoms into the last eutectic liquid is another important phenomenon that could strongly affect the properties of final solid since it is related to precipitation of second phase particles. To increase the solid volume fraction by df_s, the solidification process has to reject solute $(c_l - c_s)df_s$ with local liquid concentration c_l and solid concentration c_s. The remaining liquid is then enriched due to this rejected solute by $dc_l = (c_l - c_s)df_s/f_l$ assuming it is evenly redistributed within the liquid. With $f_s + f_l = 1$, partition coefficient $k = c_s/c_l$ and boundary condition $c_l = c_0$ at $f_s = 0$, the averaged concentration segregation c_L can be expressed as a function of the final solid fraction f_S

$$c_L = c_0(1 - f_S)^{k-1}, \tag{11}$$

which is commonly known as the Gulliver-Scheil equation [2]. It has been widely used to explain the formation of high concentration non-equilibrium phases at the late stage of solidification. However, Eq.11 does not take into account the effect of liquid pressure drop and gas phase nucleation which also happen at the late stage (or high solid volume fraction). A modification of Eq.11 that considers gas phase fraction f_g

can be written as

$$\int_{c_L^*}^{c_L} \frac{dc_l}{c_l} = (1-k)\int_{f_S^*}^{f_S} \frac{1}{1-f_s-f_g} df_s, \qquad (12)$$

where c_L^* and f_S^* are corresponding liquid concentration and solid fraction before gas phase nucleation. Since the rejected solute has to be distributed within a smaller liquid volume, Eq.12 potentially leads to a higher liquid concentration for the same solid volume fraction at the late stage of solidification. Numerical results using our PFC model clearly demonstrated this behavior in Fig.3.

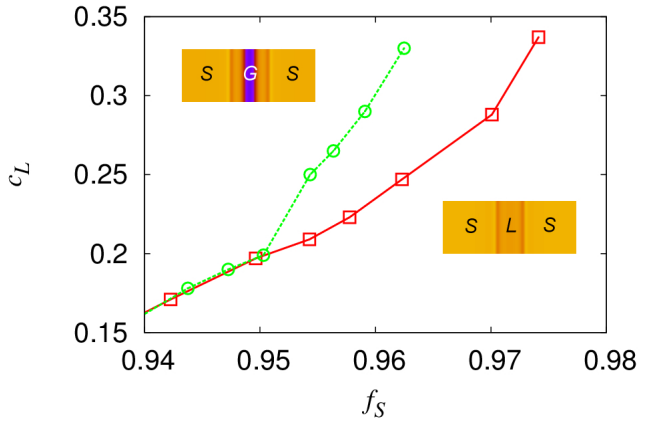

FIG. 3: Solute segregation in eutectic liquid with and without gas phase formation in late stage solidification. The two inlet figures demonstrate the system density configuration near the liquid at the highest concentration. Solid phase has the highest density and is colored as bright yellow. Gas phase has the lowest density and is colored as dark blue. Liquid is colored as dark yellow. Solid, liquid and gas phases are labeled using letter S, L, G accordingly. The top left inlet is for the top line. The bottom right inlet is for the bottom line. The simulations start with $f_L = 0.06$, $c_L = 0.15$ and liquid density $\rho_L/\rho_S = 1.0$ for the bottom line, $\rho_L/\rho_S = 0.85$ for the top line. Cooling rate $\epsilon/t = 10^{-6}$. Solute concentration is averaged over the liquid. Quasi 1-dimensional geometry similar to Fig.2 is used.

The interplay of segregation and gas phase nucleation demonstrated in Fig.3 should be most significant in deeply quenched liquid since the fast solidification rate is more likely to generate large pressure drop and cavitations. A relevant 2-dimensional scenario where a confined liquid pool is quenched below the eutectic point is investigated using this PFC model. Results in Fig.4 reveal an interesting phenomenon where the liquid cavitation is accompanied be the nucleation and growth of the second phase solid.

In summary, by incorporating density differences in multi-phase system, a novel PFC model is forged to investigate defects formation in late-stage alloy solidification. It is shown that this formulism is capable of capturing most major physics, such as solidification shrinkage, gas phase nucleation, microsegregation, elastic and plastic deformation, that are important to the late-stage solidification. It reveals an interesting interplay of microsegregation and gas phase nucleation at the late stage of solidification that can lead to second-phase solid formation near gas-phase defects. The computational model developed in this work is a fusion of most recent progresses in PFC modeling, and can be easily generalized to study the combined effect of segregation and defects nucleation in other multi-phase systems.

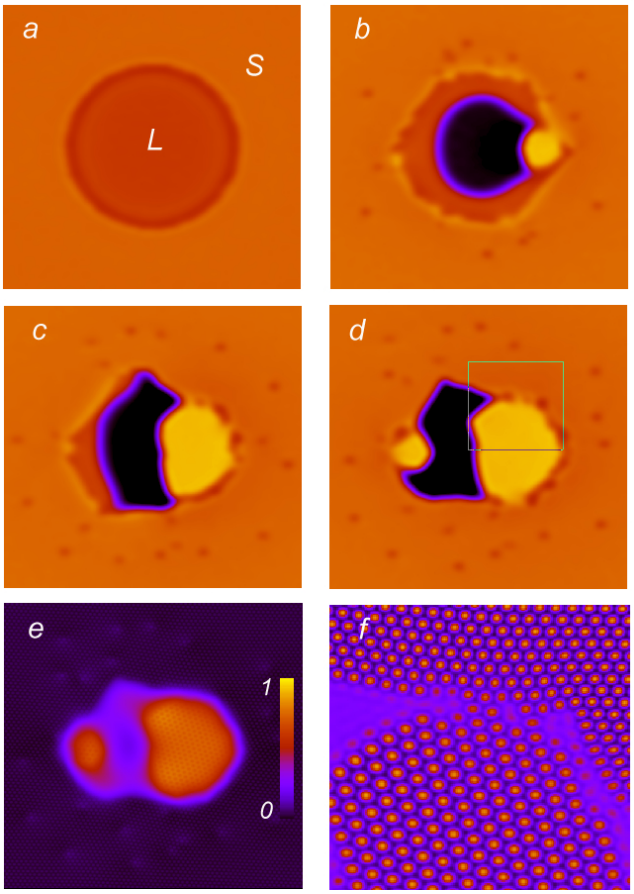

FIG. 4: Liquid cavitation is accompanied by nucleation and growth of the high concentration solid phase. (a)-(d) are density maps. (a) Liquid pool confined in the low concentration solid. The solid and the liquid regions are marked by S and L respectively. (b) Cavitation of the liquid and nucleation of the high concentration solid phase. (c) Growth of the high concentration solid. (d) Another nucleation event near the end. (e) Concentration map of (d). The color bar to the right shows the concentration scale. (f) PFC order parameter field showing different solid structures for the triple-phase region marked in (d). Note: small dark dots in the solid seen in (b)-(d) are dislocations formed during the solidification. The starting configuration is a separate liquid pool of size $R = 30a_1$ with $\rho_L/\rho_S = 0.85$, $c_L = 0.3$, $c_S = 0.07$. The system is quenched below eutectic point ($\epsilon = 0.2$)

.

We thank The National Science and Engineering Research Council of Canada for funding and Compute Canada for HPC.

[1] J. S. Langer, Rev. Mod. Phys. **52**, 1 (1980).
[2] J. A. Dantzig and M. Rappaz, Solidification, EPFL Press, 2009.
[3] W. J. Boettinger, J. A.Warren, C. Beckermann, and A. Karma, Annu. Rev. Mater. Res. **32**, 163 (2002).
[4] M. Asta, C. Beckermann, A. Karma, W. Kurz, R. Napolitano, M. Plapp, G. Purdy, M. Rappaz, R. Trivedi, Acta Mater. **57**, 941 (2009).
[5] M. Rappaz, A. Jacot, and W.J. Boettinger, Metall. Mater. Trans. A **34**, 467 (2003).
[6] D. J. Rowenhorst, J. P. Kuang, K. Thornton, P. W. Voorhees, Acta Mater. **54**, 2027 (2006).
[7] N. D. Souza, H. B. Dong, M. G. Ardakani, B. A. Shollock, Scripta. Mater. **53**, 729 (2005).
[8] A. Heckl, R. Rettig, S. Cenanovic, M. Göken, R.F. Singer J. Cryst. Growth **312**, 2137 (2010).
[9] M. Sistaninia, A.B. Phillion, J. M. Drezet, M. Rappaz, Acta Mater. **60**, 3902 (2012).
[10] David Montiel, Sebastian Gurevich, Nana Ofori-Opoku, Nikolas Provatas, Acta Mater. **77**, 183 (2014).
[11] Mingfang Zhu, Lei Zhang, Honglei Zhao and Doru. M. Stefanescu, Acta Mater. **84**, 413 (2015).
[12] A. K. Dahle, H. J. Thevik, L. Arnburg, and D. H. St. John, Metall. Mater. Trans B 287, (1999).
[13] Haifeng Wang, Feng Liu, and Gencang Yang, J. Mater. Res **25**, 1963 (2010).
[14] Yao Li, Dan Qian, Jiawei Xue, Jingchun Wan, Anfeng Zhang, Nobumichi Tamura, Zhongxiao Song, , and Kai Chen, Appl. Phys. Lett. **107**, 181902 (2015).
[15] Sander Wildeman, Sebastian Sterl, Chao Sun, and Detlef Lohse, Phys. Rev. Lett. **118**, 084101 (2017).
[16] E. Niyama, T. Uchida, M. Morikawa, S. Saito, AFS Int. Cast Metals J. 52 (1982).
[17] M. Rappaz, J. M. Drezet, M. Gremaud, Metall. Mater. Trans. A **30**, 449 (1999).
[18] J. B. Adams and W. G. Wolfer, Acta Metall. Mater. **41**, 2625 (1993).
[19] Y. Cai, H. A. Wu, and S. N. Luo, J. Chem. Phys. **140**, 214317 (2014).
[20] W. Kurz and R. Trivedi, Metall. Trans. A **22**, 3051 (1991).
[21] T. Umeda I, T. Okane I and W. Kurz , Phys. Rev. B **85**, 035449 (2012).
[22] D. Tourret, Ch.-A. Gandin, Acta Mater. **57**, 2066 (2009).
[23] O. Shuleshova, D. Holland-Moritz, W. Löser, G. Reinhart, G. N. Iles and B. Büchner, Euro. Phys. Lett, **86**, 36002 (2009).
[24] E. Nes, N. Ryum and O. Hunderi, Acta Metall. **33**, 11 (1985).
[25] N. Wang, Y. H. Wen, and L. Q. Chen, Comp. Mater. Sci. **93**, 81 (2014).
[26] N. Wang, R. Spatschek and A.Karma, Phys. Rev. E. **81**, 051601 (2010).
[27] D. M. Stefanescu, Int. J. CastMetals Res. **18**, 129 (2005).
[28] Nikolas Provatas and Ken Elder, Phase-Field Methods in Material Science and Engineering, Wiley, 2010.
[29] K. R. Elder and M. Grant, Phys. Rev. E **70**, 051605 (2004).
[30] K. R. Elder, N. Provatas, J. Berry, P. Stefanovic, and M. Grant, Phys. Rev. B **75**, 064107 (2007).
[31] Michael Greenwood, Nana Ofori-Opoku, Jörg Rottler, and Nikolas Provatas, Phys. Rev. B **84**, 064104 (2011).
[32] G. Kocher and N. Provatas, Phys. Rev. Lett. **114**, 155501 (2015).
[33] Heike Emmerich, Hartmut Lwen, Raphael Wittkowski, Thomas Gruhn, Gyula I. Tth, Gyrgy Tegze and Lszl Grnsy, Advances in Physics **61**, 665 (2012).
[34] Jesper Mellenthin, Alain Karma, and Mathis Plapp, Phys. Rev. B **78**, 184110 (2008).